THE UNIVERSITY of EDINBURGH

Edinburgh Research Explorer

Semi-automated registration-based anatomical labelling, voxel based morphometry and cortical thickness mapping of the mouse brain

Citation for published version:
Pagani, M, Damiano, M, Tsaftaris, S & Gozzi, A 2016, 'Semi-automated registration-based anatomical labelling, voxel based morphometry and cortical thickness mapping of the mouse brain', *Journal of Neuroscience Methods*. https://doi.org/10.1016/j.jneumeth.2016.04.007

Digital Object Identifier (DOI):
10.1016/j.jneumeth.2016.04.007

Link:
Link to publication record in Edinburgh Research Explorer

Document Version:
Peer reviewed version

Published In:
Journal of Neuroscience Methods

General rights
Copyright for the publications made accessible via the Edinburgh Research Explorer is retained by the author(s) and / or other copyright owners and it is a condition of accessing these publications that users recognise and abide by the legal requirements associated with these rights.

Take down policy
The University of Edinburgh has made every reasonable effort to ensure that Edinburgh Research Explorer content complies with UK legislation. If you believe that the public display of this file breaches copyright please contact openaccess@ed.ac.uk providing details, and we will remove access to the work immediately and investigate your claim.

Download date: 17. Apr. 2024

*Title page-incl. type of article and authors name and affiliation
Click here to download Title page-incl. type of article and authors name and affiliation: Pagani_Manuscript_Title_Page_so.dc

Research Article

Semi-automated registration-based anatomical labelling, voxel based morphometry and cortical thickness mapping of the mouse brain

Marco Pagani[1,2¶*], Mario Damiano[1¶], Alberto Galbusera[1], Sotirios A Tsaftaris[3&], Alessandro Gozzi[1&*]

[1] Center for Neuroscience and Cognitive Systems, Istituto Italiano di Tecnologia, Rovereto, Italy.
[2] Centro Interdipartimentale Mente/Cervello (CIMeC) - University of Trento, Rovereto, Italy.
[3] IMT Institute for Advanced Studies, Lucca, Italy.

[¶] *The two authors equally contributed to this work*
[&] *The two authors share senior authorship*

[*] **Corresponding Authors:**

e-mail: alessandro.gozzi@iit.it
e-mail: marco.pagani@iit.it

*Highlights (for review)

Highlights

- We describe registration-based methods for mouse brain morphoanatomical imaging.
- Detailed workflows for anatomical labelling, voxel based morphometry and cortical thickness are reported.
- The same preprocessing can be applied to map multiple complementary anatomical readouts.
- The present work may help to promote the use of rodent morphoanatomical imaging.

*Manuscript (With Page Numbers)
Click here to download Manuscript (With Page Numbers): Pagani_Manuscript.docx Click here to view linked References

1 **Abstract**

2 *Background*

3 Morphoanatomical MRI methods have recently begun to be applied in the mouse. However,
4 substantial differences in the anatomical organisation of human and rodent brain prevent a
5 straightforward extension of clinical neuroimaging tools to mouse brain imaging. As a result, the
6 vast majority of the published approaches rely on tailored routines that address single
7 morphoanatomical readouts and typically lack a sufficiently-detailed description of the complex
8 workflow required to process images and quantify structural alterations.

9 *New method*

10 Here we provide a detailed description of semi-automated registration-based procedures for
11 voxel based morphometry, cortical thickness estimation and automated anatomical labelling of
12 the mouse brain. The approach relies on the sequential use of advanced image processing tools
13 offered by ANTs, a flexible open source toolkit freely available to the scientific community.

14 *Results*

15 To illustrate our procedures, we described their application to quantify morphological alterations
16 in socially-impaired BTBR mice with respect to normosocial C57BL/6J controls, a comparison
17 recently described by us and other research groups. We show that the approach can reliably
18 detect both focal and large-scale gray matter alterations using complementary readouts.

19 *Comparison with existing methods*

20 No detailed operational workflows for mouse imaging are available for direct comparison with
21 our methods. However, empirical assessment of the mapped inter-strain differences is in good
22 agreement with the findings of other groups using analogous approaches.

23 *Conclusion*

24 The detailed operational workflows described here are expected to help the implementation of
25 rodent morphoanatomical methods by non-expert users, and ultimately promote the use of these
26 tools across the preclinical neuroimaging community.

27

28 **Keywords**

29 Voxel Based Morphometry; Cortical Thickness; Anatomical Labelling; Mouse Brain; MRI.

30

1. Introduction

A deep understanding of the genetic, physiological and anatomical underpinnings of brain disease is essential for the development of improved therapies. A milestone towards this goal is the generation of genetically modified mouse lines that recapitulate targeted genetic mutations in experimentally controlled studies. Genetically modified mouse lines permit to relate genetic mutations to clinically relevant endophenotypes without the complexity of genetic heterogeneity and the uncontrolled impact of gene-gene and gene-environment interactions in adult human populations (Nestler and Hyman, 2010).

Magnetic resonance imaging (MRI) methods offer a privileged point of view to study genetically altered mouse models of neuropsychiatric disorders in many respects. First, the use of comparable imaging readouts in men and mice permits a cross-species comparison of brain endophenotypes of translational relevance, thus enhancing the transfer of information from and to the clinic. At the same time, MRI readouts can also be employed to assess the extent to which mouse models of central nervous system pathology replicate neuroimaging findings observed in clinical populations, informing preclinical researchers on the translational validity of these models. Moreover, high resolution morphometric MRI, achievable at ultra-high field strength or in *ex vivo* formalin-fixed samples (Lerch et al., 2012; Tucci et al., 2014) can be employed to obtain a fine-grain assessment of structural brain alterations that could serve as a convenient surrogate for labour intensive manual morphometric measurements in *ex vivo* brain slice preparations, with the additional advantage of being non-invasive and multi-dimensional.

Structural MRI based imaging methods - such as voxel based morphometry (VBM) of gray matter (GM), cortical thickness mapping and anatomical labelling - have been widely employed to study brain morphology in human populations (Mueller et al., 2012). The application of analogous readouts to map genetically determined brain alterations in transgenic mouse lines has been recently proposed, an effort collectively referred to as MRI phenotyping (Borg and Chereul, 2008; Johnson et al., 2007; Lerch et al., 2011a). Recent improvements in MRI sequences and hardware, together with the development of fixation protocols for *ex vivo* imaging of stained brain specimens (Lerch et al., 2012), have made it possible the acquisition of artefact-free and high resolution – with a voxel size less than 80 µm – mouse brain volumes even at relatively low magnetic field strengths. This efforts have resulted in the publication of several examples or the application of morphoanatomical imaging to transgenic mouse models (Lerch et

62 al., 2008; Sawiak et al., 2009; Xie et al., 2010; Yushkevich et al., 2006).

63 The development of standardised preprocessing and analytical pipelines for human 64 imaging data, and their implementation in popular software toolkits such as such as FMRIB 65 Software Library (FSL) (Jenkinson et al., 2012), Statistical Parametric Mapping (SPM) (Friston 66 et al., 1994) and Advanced Normalization Tools (ANTs) (Avants et al., 2009), have been 67 instrumental to the widespread use of MRI in human brain research. However, substantial 68 differences in the dimensions and anatomical organisation of the human and rodent brain prevent 69 a straightforward extension of these tools to morphoanatomical mouse brain mapping. As a 70 result, several research groups have developed tailored procedures for the preprocessing and 71 analyses of morphoanatomical brain MRI readouts in mouse models (Badea et al., 2012; Borg 72 and Chereul, 2008; Delatour et al., 2006; Johnson et al., 2007; Lee et al., 2010; Lerch et al., 73 2011a; Nieman et al., 2005; Sawiak et al., 2009; Sawiak et al., 2013). However, the vast majority 74 of the published approaches typically address single morphoanatomical readouts (e.g., VBM *or* 75 anatomical labelling *or* cortical thickness), and lack a detailed description of the complex 76 workflow and computational parameters required to process, analyse and quantify structural MRI 77 alterations, thus complicating the implementation of these procedures by non-expert users.

78 To begin to address these issues, here we provide a detailed methodological description 79 of a semi-automated operational workflow for VBM, cortical thickness estimation and automated 80 anatomical mapping of the mouse brain. To simplify and streamline operations, we based image 81 processing mainly on ANTs (Avants et al., 2009), a flexible and powerful open source toolkit 82 freely available to the scientific community. Importantly, our approach has been recently applied 83 by our research group to map fine-grain brain anatomy alterations in different mutant mouse 84 lines (Dodero et al., 2013; Lassi et al., 2015; Minervini et al., 2014; Sannino et al., 2014; Tucci et 85 al., 2014) and to describe large-scale networks of anatomical covariance between gray matter 86 regions in wild-type mice (Pagani et al., 2016), with excellent agreement between MRI and 87 manual morphometric measurements (Sannino et al., 2014), exhibiting corresponding 88 morphoanatomical features in mice and reference clinical populations (Cutuli et al., 2016; Tucci 89 et al., 2014). Below, we provide a detailed description of our procedural workflow and show its 90 capabilities by describing its application to quantify morphological alterations in socially-91 impaired BTBR T+Itpr3tf/J mice with respect to normo social C57BL/6J controls (Dodero et al., 92 2013; Squillace et al., 2014), a comparison that has been recently described by our research

group (Dodero et al., 2015) and others (Ellegood et al., 2013), thus permitting an empirical cross-laboratory assessment of the validity of our findings.

2. Materials and Methods

2.1. Ethical statement

All *in vivo* studies were conducted in accordance with the Italian law - D.L. n° 116, 1992, Ministero della Sanità, Roma - and following the recommendations in the Guide for the Care and Use of Laboratory Animals of the National Institutes of Health. The animal research protocol was approved by the Animal Care Committee of the Istituto Italiano di Tecnologia (Permit Date 07-2012). All surgical procedures were performed under deep anaesthesia.

2.2. Sample Preparation and MR acquisition

High-resolution morphoanatomical T2-weighted MR imaging of mouse brains was performed in paraformaldehyde (4% PFA; 100 ml, Sigma, Milan) fixed specimens, a procedure employed to obtain high-resolution images with negligible confounding contributions from physiological or motion artefacts (Cahill et al., 2012). Sample preparation and MRI acquisition of BTBR T+Itpr3tf/J (BTBR) and C57BL/6J (B6) mice has been recently described in previous work (Dodero et al., 2013; Sforazzini et al., 2014a; Sforazzini et al., 2014b) and is briefly summarised here. Male BTBR (N=9, 15-26 weeks old) and age-matched control B6 (N=9) mice were deeply anaesthetized with an intraperitoneal Avertin injection (375 mg/Kg, Sigma, Milan) and their brains were perfused *in situ* via cardiac perfusion. The perfusion was performed with phosphate buffered saline followed by paraformaldehyde (4% PFA; 100 ml). Both perfusion solutions were added with a Gadolinium chelate (Prohance, Bracco, Milan) at a concentration of 10 and 5 mM, respectively, to shorten longitudinal relaxation times (Lerch et al., 2012).

A multi-channel 7.0 Tesla MRI scanner (Bruker Biospin, Milan) was used to acquire anatomical images of the brain, using a 72 mm birdcage transmit coil, a custom-built saddle-shaped solenoid coil for signal reception, and the following imaging parameters: 3D RARE spin-echo sequence, TR=550 ms, TE=33 ms, RARE factor=8, echo spacing 11ms, matrix size of 192x 170x170 and voxel size of 0.09 mm (isotropic), with a total acquisition time of 4 hrs and 25 mins.

124

125 **2.3. Image preprocessing and analysis**

126 A detailed description of the image processing workflow employed to create a study
127 based template, to estimate cortical thickness, and to perform automated anatomical labelling and
128 VBM is reported below for structural images acquired at 7 Tesla. We refer to our approach as
129 "registration-based" as several preprocessing and estimation steps (e.g., cortical thickness) are
130 executed via a combination of affine and symmetric diffeomorphic transformations as
131 implemented in *antsRegistration* command (Avants et al., 2014). The tool entails the application
132 of affine registration with twelve degrees of freedom to coarsely normalise the overall shape of a
133 source image to a reference image. Afterwards, a non-linear transformation is applied to create a
134 differentiable and invertible diffeomorphic map which locally aligns source and reference image
135 by adjusting for local inter-individual morphological differences.

136 Flowcharts are provided as a visual reference to guide the description of each
137 computational step, where light grey shading denotes image inputs, dark grey shading denotes
138 the final output and computational processes are outlined in the form of rectangular boxes. All
139 the computational steps have been carried out using tools and algorithms implemented within the
140 ANTs toolkit (version 1.9 http://sourceforge.net/projects/advants/) and employed to process 3D
141 RARE morphoanatomical images acquired at 7 Tesla with the image sequence parameters
142 described above. The parameter employed for the preprocessing steps were optimized in pilot
143 assessments using both empirical (e.g. segmentation) and quantitative approaches (e.g.
144 registration).

145

146 *2.3.1. Image preprocessing*

147 Basic image preprocessing includes bias field correction and skull stripping (Figure 1).
148 As a first step, all the images are corrected for intensity non-uniformity using
149 *N3BiasFieldCorrection,* an automated algorithm implemented within the ANTs toolkit using 50
150 fitting levels. This step reduces bias field signal related to the reception profile of MRI receive
151 coils, a low frequency amplitude modulation of the signal that produces regional variation in
152 voxel intensity as a function of coil proximity. The correction of this bias is an important pre-
153 requisite for subsequent intensity based MR image processing, such as tissue segmentation.

154 Skull stripping is required to remove extra brain tissue, thus crucially improving the

155 accuracy of subject-to-template registration. In order to automate skull-stripping and avoid
156 tedious and error-prone manual segmentation, an automatic registration-based approach to skull
157 stripping was devised. This is carried out by registering the bias adjusted MRI volumes to a skull
158 stripped reference image using an affine and diffeomorphic registration algorithm. The skull
159 stripped reference image should ideally be chosen from the study population or from comparable
160 experiments of the same laboratory. A companion brain binary mask of the reference image can
161 be segmented manually. While potentially labour intensive in high resolution brain images, this
162 process can be performed only once, and it is instrumental to automating skull stripping for all
163 the subsequent subjects and analyses. After the registration, the diffeomorphic map is applied to
164 non-linearly transform the brain mask of the reference image into the subjects' space using
165 *WarpImageMultiTransform*. The subject's brain mask is then applied to each original subject
166 image to obtain skull stripping. An additional bias correction is subsequently performed on the
167 skull stripped subject image to achieve a more accurate estimation of the bias field, devoid of the
168 contribution of non-brain related protrusions.

169 An illustrative example of the advantage of performing two independent bias corrections,
170 (before and after skull stripping, respectively) is reported in Figure 2. Even though the first step
171 does not flawlessly compensate for signal inhomogeneity in all brain regions (i.e. the ventral
172 areas of the brain and in the ventricles), its use provides a first normalization of signal intensity
173 that results in an improved the accuracy of registration based estimation of brain mask, and the
174 removal of brain extra tissue. After this skull stripping step, the bias field of the original subject
175 image is re-estimated, leading to a more accurate bias correction. The results of this first-pass
176 skull stripping are typically visually inspected for imperfections, usually present in a minority of
177 subjects, which can be easily manually corrected, for example using the brushtool of ITKsnap
178 (Yushkevich et al., 2006). For each subject, the result of preprocessing is a skull stripped and
179 bias corrected brain image, exhibiting uniform contrast within the same tissue class, and its
180 binary mask.
181

182 *2.3.2. Study based template*

183 A critical element in our approach is the construction of a study based template to
184 establish a common reference space for all the subsequent analyses. In cross-sectional mouse
185 studies, the most adopted experimental designs for mouse phenotyping with transgenic lines, this

186 involves the creation of an average template from a reference population, typically the control
187 subjects (B6 in this study). This leads to the generation of a template recapitulating
188 neuroanatomical features of "healthy" or reference population, avoiding the combination of
189 conflicting morphoanatomical traits which could affect subsequent computational steps (e.g.
190 segmentation). For example, the use of both normo-callosal B6 and acallosal BTBR mice for
191 template creation would result in a chimeric image exhibiting a blurred and hypo-intense corpus
192 callosum, a feature that could negatively affect the quality of subsequent segmentation priors.
193 The creation of different templates for different studies can help minimizing confounding effects
194 related, for instance, to perfusion, age, sex and brain sizes.

195 Study-based template creation was implemented via the use of the *buildtemplateparallel*
196 script available within the ANTs toolkit (Avants et al., 2010b). This script entails an automated
197 and iterative intensity-based registration approach to automatically create a study based template
198 using a predefined list of subjects (Kovacevic et al., 2005). A representative subject is selected as
199 initial reference and each subject is linearly registered to the reference subject using an affine
200 transformation. After intensity averaging all registered images to obtain a first linear group
201 average, an iterative five-generation multi-scale non-linear alignment process is performed using
202 a *Greedy Syn* diffeomorphic registration algorithm (Avants et al., 2008) with a maximum of 120
203 iterations for each step. This process entails an initial diffeomorphic registration of each subject
204 to the reference linear group average to obtain individuals' warps using cross correlation as
205 similarity metric. These warps are then averaged and applied to the template to update its shape
206 and conform it to the population shape. The process is iteratively repeated four more times, by
207 using as reference the warped template from the previous iteration. The final outcome is an
208 average template volume exhibiting clear structural boundaries, incorporating fine grain
209 neuroanatomical descriptions of the reference population, and reduced intensity variation.
210
211 *2.3.3. Anatomical labelling*

212 The assessment of subtle anatomical differences in gross morphology via manual delineation
213 of brain structures is a laborious and time consuming task that may introduce intra- and inter-
214 observer bias (Badea et al., 2012). The procedures described here allows for volumetric
215 estimation via anatomical labelling, a procedure whereby brain regions can be labelled and
216 classified depending on their anatomical location. The process employed in our workflow relies

217 on the availability of preprocessed images, a study-based template and two neuroanatomical
218 labelled reference MRI atlases for cortical (Ullmann et al., 2013) and subcortical (Dorr et al.,
219 2008) areas, respectively. The output of automated anatomical labelling is a fine-grained
220 projection of a given anatomical label in the subject's coordinate space. The anatomical labels
221 thus registered can be used both to measure the volume of anatomical regions of interest for
222 cross-strain statistical comparison, or as intermediate input for further analyses, such as cortical
223 thickness estimation (Figure 3).

224 The volume of specific anatomical regions in individual subjects is computed using a
225 template based anatomical labelling strategy (Avants et al., 2010b). As previously reported in
226 the literature, the propagation of labels from the anatomical labelled atlas to the subject space is
227 more accurate when performed via the study based template to minimize variation due to
228 registration errors (Jia et al., 2011). To this purpose, a composition of affine and diffeomorphic
229 (SyN) registration between the reference neuroanatomical atlas and the study based template is
230 performed to project the anatomical labels in the coordinate system of the study based template
231 (Avants et al., 2009) For the anatomical images and RARE sequence used in this study we
232 adopted cross correlation as similarity metric, with a window radius of 5 and a gradient step
233 length of 0.25. The optimisation was performed over four resolutions for both transformations
234 with a maximum of 100 iterations for the coarse levels and 10 at the full resolution. A simple
235 propagation of the neuroanatomical labels mapped in the study-based template space to the
236 subjects' space can then be achieved via the registration of each subject to the study based
237 template and the subsequent propagation of the labels to each subject. The efficiency of the
238 registration procedures can evaluated using the Dice coefficient (*DiceAndMinDistSum* command
239 from *ImageMath)*, which quantifies the overlap between a manually defined label and the same
240 label resulting from our automated labelling, in the subject space (Dice, 1945). Label volumes
241 can then be easily computed using tools included in several MRI software packages (e.g.
242 *LabelStats* command from *ImageMath,* or FSL's *fslstats*).

243

244 *2.3.4. VBM*

245 VBM is a whole-brain technique for characterizing regional brain volume and differences
246 in tissue concentration, in particular GM, across subjects. In our procedure, it consists of five
247 main steps (Figure 4).

248 First, a study based template is created using brain anatomical images from reference
249 population described above. Second, the original images of the two groups of subjects are
250 registered to the study based template via the same affine and diffeomorphic mapping used for
251 anatomical labelling. Third, spatially normalized images are segmented using a Markov Random
252 Field model, implemented by the *Atropos* command of the ANTs toolkit (Avants et al., 2011).
253 To classify tissues we applied a smoothing factor of 0.0125, a radius of 1 and the maximum
254 number of iterations was set at 10. The separation of GM (i.e. the readout of interest) from white
255 matter (WM) and cerebrospinal fluid (CSF) is improved by initializing the process with the study
256 based template, previously segmented using standard k-means clustering included in the *Atropos*
257 command. (Figure 5, B-C). This step is especially critical and it is therefore here described in
258 greater detail. In pilot work, we explored the number of tissue classes leading to optimal
259 separation of GM from non-GM components (WM plus CSF). A canonical three-class
260 segmentation of *ex vivo* mouse brain using *Atropos* results in inefficient GM/WM segmentation,
261 leading to an overestimation of WM fraction at the expense of GM (Figure S1). The use of six
262 independent classes results in three GM clusters that can be merged to provide a final accurate
263 GM map (Fig. 5). A similar approach has been employed by other investigators (e.g. (Li et al.,
264 2009)). Our segmentation procedure results in a two-voxel layer on the outmost edge of the
265 cortex which is labelled as "non gray matter" and, as such, is not included in subsequent
266 analysis. These voxels are characterised by low or very-low signal intensity and reflect a
267 combination of partial volume effects between gray matter and non MRI visible skull signal, and
268 possibly also small inaccuracies due to registrations. In our workflow, these "low confidence"
269 gray matter voxels are discarded to improve the robustness of subsequent voxelwise statistical
270 mapping.

271 In our procedure, the quality of segmentation is assessed empirically by comparing
272 individual and merged tissue classes with the anatomical distribution of known high-density WM
273 structures such as the corpus callosum, anterior and posterior commissures, as seen in the study
274 based template (Figure 5). These structures are easily identifiable and their extension can be
275 compared with their segmented counterparts. Future developments of our initial workflow could
276 employ quantitative approaches to estimate goodness of cluster separation (Chou et al., 2004;
277 Wu and Yang, 2005), although operator dependent assessments of tissue class separations are
278 ultimately warranted to ensure biologically meaningful results.

279 It should be noted that the segmentation procedure employed in our work does not always
280 lead to a clear separation of WM and CSF, at least on brain volumes acquired *ex vivo*. Besides
281 differences in the anatomical organization of the mouse brain and image contrast in the PFA
282 perfused brain (Cahill et al., 2012), a contributing reason for this is the occurrence of CSF loss
283 from the brain in a large proportion (ca. 70%) of the subjects as a consequence of the *ex vivo*
284 fixation procedure, leading to the presence of signal voids in ventricular space. These low signal-
285 intensity intra-ventricular foci are typically classified as WM, leading to mixed or incomplete
286 separation between these two brain components. Such incomplete separation however does not
287 limit the validity of our approach, because both CSF and WM (even if separate) would invariably
288 end up being discarded from subsequent GM-based analyses (i.e. VBM and cortical thickness).
289 After tissue segmentation, the Jacobian determinants of the deformation are calculated with
290 *ANTSJacobian* command of the ANTs toolkit and used to modulate the GM probability maps
291 calculated during the segmentation step. This step permits the analysis of GM probability maps
292 in terms of local anatomical variation instead of tissue density (Ashburner and Friston, 2000).
293 Jacobian determinants can be also normalized by the total intracranial volume to further
294 eliminate overall brain volume variations and calculate relative GM volumes. Fifth, the resulting
295 modulated GM probability maps are smoothed using a Gaussian kernel with a sigma of three
296 voxel width (FWHM=0.64mm) and employed for voxel-wise statistical comparison.
297
298 *2.3.5. Cortical Thickness*
299 The proposed registration-based cortical thickness *DiReCT* estimation approach (Figure
300 3) is a voxelwise computational approach based on the method presented by Das and colleagues
301 (Das et al., 2009) and relies on the *KellyKapowsky* command within ANTs toolkit. The method
302 provides cortical thickness measurements at the voxel level using cortical and non-cortical
303 labelled volumes as inputs. From an anatomical standpoint, the cortical labelled volume
304 employed (cortical ribbon) is limited between an external outline corresponding to the outer
305 layer of the cortex and an internal outline identified by the inner layer of the cerebral cortex
306 adjacent to callosal WM fibres. The method identifies a continuous one-to-one correspondence
307 between inner and outer cortical surfaces and the cortical thickness is estimated via a distance
308 measure on the basis of this diffeomorphic correspondence. The inner surface is used as a
309 reference to initialize a thin layer of about 1 voxel width. This layer, which replicates the shape

310 of the outer layer of the cortex, is then allowed to expand under the diffeomorphic deformation.
311 The deformation is introduced through the cortical label until the layer reaches the outer cortical
312 surface and the obtained deformation map can eventually be used to compute the cortical
313 thickness. The final result of this process is a cortical voxelwise map with a nominal "thickness"
314 value in each voxel, reflecting the deformation field that voxel has been subjected to (Das et al.,
315 2009). Figure S2 shows an illustrative example of the obtained voxelwise cortical thickness map
316 where the presence of parallel columns of voxels exhibiting constant thickness is apparent. The
317 obtained maps are then typically cross-compared using standard voxelwise statistics. The
318 original method (Das et al., 2009) was optimized to identify deep sulci of the human brain by
319 forcing the algorithm to recover lost sulci, but can also be applied to map lissencephalic cortices
320 like those of the rodent brain. The estimation process is carried out separately for right and left
321 hemisphere to preserve the Neumann boundary (Lee et al., 2011).

322 The cortical thickness estimation includes four main steps. First, a right and the left
323 cortical label need to be created, as well as the non-cortical label. In the present study this was
324 achieved by combining all cortical labels mapped (enthorinal cortex, frontal, occipital and
325 parieto-temporal lobe) of the Dorr MRI atlas of the mouse brain (Dorr et al., 2008) into one
326 single hemispheric label. A non-cortical label was generated by merging all the remaining non-
327 cortical regions. Second, cortical thickness is estimated using *KellyKapowsky*, with a prior
328 anatomical constraint of cortical thickness of two millimetres and a gradient step size for
329 optimisation of 0.02. Number of iterations, threshold and window size for convergence were left
330 unchanged (e.g. default parameters). Third, maps of cortical thickness are combined into a joint
331 volume and transformed to template space using available registration maps obtained previously.
332 Fourth, the transformed cortical maps are smoothed using a Gaussian kernel with a sigma of two
333 voxel width (FWHM=0.42). This process yields images that can be used for univariate or
334 multivariate analysis at the voxel level.

335 Despite the use of non-callosal mice our automated anatomical labelling correctly
336 labelled the cortical mantle of BTBR in virtually all cortical areas, with possible minor
337 underestimations of cortical thickness in medial anterior cingulate regions. As a result,
338 intergroup alterations in those regions may be interpreted cautiously when acallosal mice are
339 used as reference strain. However most mouse lines commonly used in neuroscience and
340 preclinical research exhibit normal callosal integrity and are therefore to be considered immune

341 to this potential artefact.

342 To further evaluate the accuracy of the cortical thickness estimation process, manual 343 measurement was also performed by an experienced operator blinded to the results of the cortical 344 thickness estimation (Figure 6). In a randomly chosen subject, three coronal slices were extracted 345 and cortical thickness was measured for secondary motor cortex (M2), secondary somatosensory 346 cortex (S2) and auditory cortex (Au) using the ruler tool available in the ITK Workbench.

347

348 **2.4. Statistical analysis**

349 All statistical analysis of the smoothed and modulated GM probability maps and cortical 350 thickness maps were conducted using FSL. Firstly, maps were concatenated in a 4D dataset, 351 using *fslmerge*. Subsequently, standard non-parametric Monte Carlo test with 5000 random 352 permutations was performed using *randomise*. Threshold-free cluster enhancement was 353 employed to include voxels' neighbourhood information without defining a-priori cluster 354 threshold. P-values were corrected for multiple comparisons using a cluster-based threshold of 355 0.01 (Jenkinson et al., 2012; Worsley et al., 1992). Two-tailed voxelwise statistics were used for 356 inter-group VBM and cortical thickness mapping. Brain volumes, resulting from the 357 segmentation process, were tested for statistical differences between the two strains using a two-358 tailed Student's t-test, followed by Hochberg's correction for multiple comparisons.

359

360 **3. Results**

361 As an illustrative example of the approach, we tested our set of methods to map and 362 quantify morphological variations in inbred socially impaired BTBR mice with respect to 363 normosocial B6 (Squillace et al., 2014). A biological interpretation of the differences mapped 364 has been recently reported by us (Dodero et al., 2013) and others (Ellegood et al., 2013), and will 365 not be re-discussed here.

366

367 *3.1. Study based template and volumetric analysis*

368 A study based template created following the procedure herein explained is depicted in 369 Figure 5. The template was created using the scans of nine normosocial B6 mice, which have 370 been used as reference population for this illustrative study. The template reveals clear structural 371 boundaries and high WM-GM contrast, depicting fine-grain anatomical features that can be used

372 to describe the population more effectively and reliably than a single representative subject
373 (Tucci et al., 2014).

374 In pilot studies, we assessed the accuracy of registrations as a function of varying
375 registration parameters (i.e. window radius and gradient step for symmetric normalization) as
376 recently described (Badea et al., 2012). By varying registration parameters, the approach can be
377 used to identify the best set of parameters matching the results of manual parcellation. We varied
378 windows radius between 3 and 9 voxels, and gradient step for symmetric normalization between
379 0.10 and 2 voxels. The results of this analysis (Figure S3) show that the parameters choses (5 and
380 0.5 voxels, respectively) produce a good registration accuracy in all the brain regions tested.
381 These parameters are in agreement with those previously selected by Badea and colleagues using
382 *ex vivo* brain samples imaged at 9.4 Tesla.

383 Using these validated parameters, cross-strain volumetric analysis using anatomical
384 labels from the two atlases highlighted the presence of a general reduction in cortical volume in
385 BTBR mice with respect to B6 mice. Also major subcortical structures, including caudoputamen,
386 hippocampus and hypothalamus reported a statistical significant reduction in volume (Figure 7).
387 These results are in good agreement with recent comparative neuroanatomical mapping of these
388 two strains performed by other labs (Ellegood et al., 2013), where a similar significant decrease
389 in the volume of cortex and corpus callosum was shown.
390
391 *3.2. VBM*
392 Whole-brain VBM revealed widespread and bilateral reductions in GM volume across
393 dorsofrontal, cingulate, retrosplenial, occipital and parietal cortex (Figure 8, $Z>3.1$, p-
394 corrected$<.001$), in BTBR compared to B6 controls. These findings are in agreement with the
395 results of anatomical labelling. GM volume reductions were also evident in subcortical areas,
396 including the lateral and posterior thalamus (longitudinal fasciculus), the posterior hypothalamus
397 and the ventral hippocampus. Interestingly, VBM highlighted also small bilateral foci of
398 increased GM volume in the olfactory bulbs, in the medial pre-frontal and insular cortex, in the
399 amygdala and in the dorsal hippocampus. The detection of small focal effects that could not be
400 revealed when integrated over large anatomical volumes is one of the main advantages of the
401 VBM approach over classic neuroanatomical volumetric mapping. These results are in good
402 agreement with recent comparative neuroanatomical mapping of these two strains performed by

403 other labs using tensor based morphometry (Ellegood et al., 2013), which showed similar
404 significant alterations (using Tensor Based Morphometry, see discussion below) in hippocampal
405 and cortical areas.
406
407 *3.3. Cortical Thickness Estimation*
408 Further investigation of the presence of local alterations of GM in BTBR mice compared
409 to B6 controls was performed in terms of cortical thickness estimation. Average spatially-
410 normalized voxel-based thickness maps were calculated separately for each of the two strains
411 and three-dimensionally rendered for visualization purposes (Figure 9). In good agreement with
412 the results of automated anatomical labelling and VBM mapping, a widespread reduction in
413 mean cortical thickness ($Z>2.3$, p-corrected<0.01) was observed in BTBR mice compared to B6
414 controls. Importantly, inter-group voxel-wise statistics revealed significantly increased cortical
415 thickness in medial prefrontal and insular regions in the BTBR cohort ($Z>2.3$, p-corrected<0.01).
416
417 **4. Discussion and conclusions**
418 Here we described semi-automated procedures for automated anatomical labelling, VBM
419 and cortical thickness estimation in the mouse brain. The approach has been recently applied to
420 detect fine-grained morphoanatomical alterations in different mutant mouse lines, including
421 alterations in β-catenin mouse mutants (Tucci et al., 2014), acallosal and socially-impaired mice
422 (Dodero et al., 2013) and to identify sexually divergent effects on cortical anatomy in catechol-
423 O-methyltransferase mutant lines (Sannino et al., 2014). In the latter study, we showed
424 remarkably consistent intergroup differences in regional GM volume as assessed with our VBM
425 pipeline, or manual morphometric measurements of cortical thickness in post-mortem brain
426 slices (Sannino et al., 2014), thus underscoring the accuracy and sensitivity of our workflow.
427 The image processing described here adopts the methodologies and toolkits originally
428 developed for human brain imaging and can be straightforwardly extended to other areas of
429 research and mouse models of disease. For example, we also used VBM to describe symmetric
430 networks of anatomical covariance in the cortex of inbred mice complementary to those
431 previously identified in humans, providing a new tool to study gray matter disrupted connectivity
432 in brain disorders with transgenic mice (Pagani et al., 2016). Although prominent examples of
433 the use of morphoanatomical methods in the mouse have been recently described by other labs

434 (Badea et al., 2012; Borg and Chereul, 2008; Budin et al., 2013; Delatour et al., 2006; Johnson et
435 al., 2007; Lee et al., 2010; Lerch et al., 2011a; Nieman et al., 2005; Oguz and Sonka, 2014;
436 Sawiak et al., 2009; Sawiak et al., 2013), the vast majority of these contribution lack a detailed
437 description of the complex workflow required to process and analyse different
438 morphoanatomical readouts, thus complicating the replication of these methods by other groups.
439 The methodological workflow presented in this work was designed to facilitate the
440 implementation of fine-grained morphoanatomical mapping tools by non-expert users, and
441 promote forward and back translation of MRI preclinical and clinical research evidence. We also
442 point out that a preliminary account on the implementation of these procedures in parallel
443 computing cloud environment has been recently reported (Minervini et al., 2014), a strategy that
444 can streamline and accelerate image processing time by exploiting large high-performance-
445 computing infrastructures.

446 A dominant feature of our unified approach is the coupling of standard intensity based
447 affine registration with a symmetric diffeomorphic normalization algorithm to obtain optimal
448 MR image registration (Avants et al., 2008). This approach, which has been successfully
449 employed both in human (Kim et al., 2008; Klein et al., 2009; Klein et al., 2010) and small
450 animal imaging studies (Avants et al., 2010b; Lerch et al., 2011b), is based on the ANTs open
451 source software library and is adopted to create a study based template, carry out skull stripping
452 and perform anatomical labelling via label propagation. Our cortical thickness estimation
453 approach is also registration-based, and employs *DiReCT*, an advanced diffeomorphic
454 registration algorithm implemented in ANTs toolkit that has been recently validated on human
455 imaging data (Das et al., 2009) and used for research studies with clinical population (Avants et
456 al., 2010a). To the best of our knowledge, this is the first example of the application of this
457 approach to map cortical thickness in small rodent species.

458 The cortical thickness mapping and anatomical labelling approaches employed rely on
459 the availability of three dimensional labelled MRI atlases with delineated cortical and subcortical
460 morphology. While a universally accepted MRI atlas of the mouse brain is still not available, a
461 number of mouse brain MRI atlases have been published based on high resolution acquisitions of
462 a single subject (Badea et al., 2012; Maheswaran et al., 2009a; Xie et al., 2010; Zhang et al.,
463 2010) or constructed from several animals, with data gathered either *in vivo* (Aggarwal et al.,
464 2009; Ma et al., 2008; Maheswaran et al., 2009b) or from *ex vivo* fixed specimens (Aggarwal et

465 al., 2009; Badea et al., 2007; Dorr et al., 2008; Johnson et al., 2010; Kovacevic et al., 2005;
466 Ullmann et al., 2013). In this study, a combination of two atlases was employed to obtain a fine-
467 grained parcellation of both cortical (Ullmann et al., 2013) and subcortical (Dorr et al., 2008;
468 Ullmann et al., 2013) regions. However, our method is not atlas-dependent and can be flexibly
469 adapted to a number of published or custom mouse brain MRI anatomical partitions.
470 An important benefit of our approach is the possibility to measure different and
471 complementary morphoanatomical brain metrics - including volumetric analysis, VBM and
472 cortical thickness - in a single reference space. This aspect is of crucial importance, as it
473 broadens the scope of application of MRI-based brain morphometry and it augments its
474 translational potential by permitting a multi parametric comparison with analogous clinical
475 readouts. In the illustrative example reported here, an overall agreement between the three
476 readouts was found. Apparent discrepancies between readouts (e.g., the lack of inter-strain
477 differences in insular volume, due to the presence of VBM foci of increased and decreased
478 regional volume in anterior and posterior portions of this region) are the result of different
479 sampling scales (label vs. voxel level) of the readouts employed. We also note that the
480 combination of complementary approaches can help disambiguate morphological alterations of
481 pathological origin, as the relationship between thickness and local GM volume has not been
482 thoroughly clarified, and may probably change across pathologies and populations (Hutton et al.,
483 2008). Within this scenario, the use of complementary metrics coupled to histological staining
484 can help to pinpoint the pathological bases of brain morphometric changes of neuropathological
485 origin.
486 In addition, our preprocessing workflow can be straightforwardly extended to perform
487 tensor based morphometry (TBM). As in VBM, TBM entails the local computation of the
488 Jacobian determinants of the deformation field used to map subjects' images to the study based
489 template. The Jacobian determinant (i.e. the local scaling factor) encodes for local anatomical
490 expansions and contractions of subjects' areas relative to the study based template, and therefore
491 Jacobian maps can be used to localise inter-group differences in the local shape of brain
492 structures at the voxel level. TBM analysis can be simply performed by omitting the tissue
493 segmentation step in the VBM procedure herein described. As TBM does not entail tissue
494 classification, it can be used for the simultaneous investigation of WM and GM alterations, and
495 may robustly detect alterations in areas of mixed WM-GM structures, such as the thalamus and

496 brain stem, which are especially sensitive to the accuracy of intensity based tissue classification
497 algorithms.
498 A few methodological limitations in our approach deserved to be mentioned. The
499 procedure described here has been developed and optimized or fixed *ex vivo* brain samples
500 imaged at 7 Tesla using T2-weighted images. While the application of our workflow to different
501 field strengths and image contrast is conceivable, adjustments in single preprocessing parameters
502 may be required to adapt our procedure to different contrast mechanisms or images acquired at
503 different field strengths. One limitation of our cortical thickness mapping is its poor performance
504 in resolving thickness at the level of inter-hemispheric fissure in medial regions of the mouse
505 cortex such as cingulate or retrosplenial areas (Figure S2). As a result, inter-group differences in
506 cortical thickness in these regions should be interpreted with caution. Researchers interested in
507 mapping gray matter alterations in these regions with high confidence, should consider cross
508 validating thickness mapping with voxelwise methods described in our workflow that are
509 immune to this limitation, such as VBM and TBM. Similarly, the segmentation of the anterior
510 cingulate in acallosal mice such as BTBR should be considered tentative, as the lack of clear
511 white matter gray matter boundary prevents an empirical assessment of its accuracy. Once again,
512 voxelwise-based morphoanatomical mapping together with histological measurements can help
513 validate cortical thickness measurements in these areas when acallosal mice are employed.
514 Caution should also be exercised in interpreting inter-group differences in mouse models
515 characterized by profound demyelination and neurodegeneration, two conditions that can reduce
516 GM/WM contrast and affect segmentation accuracy for VBM. Notwithstanding these limitations,
517 the possibility of using a unified workflow to map multiple complementary morphoanatomical
518 parameters should be emphasized as a major point of strength of our approach, owing to the
519 possibility of cross-comparing different readouts to dissect specific neuroanatomical features
520 with increased confidence.
521 In conclusion, we described a registration-based approach for anatomical mapping, VBM
522 and cortical thickness estimation in the mouse brain. The application of these procedures enabled
523 the identification of subtle volumetric differences across subjects without prior knowledge of
524 structures of interest. Our unified approach based on diffeomorphic registration permits to
525 integrate complementary MR morphoanatomical techniques, and is based on popular open
526 source software (ANTs), which has been extensively employed in priori MRI morphometric

527 studies. The detailed operational workflow described in the present work is expected to help the
528 implementation of rodent morphoanatomical methods by non-expert users, thus ultimately
529 promoting the use of these tools across the preclinical neuroimaging community.
530

531 ## Captions
532

533 **Figure 1. Preprocessing workflow.**

534 Each MRI subject image undergoes a first correction for intensity non-uniformity bias using the
535 *N3BiasFieldCorrection*. To create individual subject masks, a masked representative reference subject is registered
536 to each subject, and the transformation of this registration is then applied to the reference subject mask. The
537 application of this mask permits to remove most extra brain tissue. Non-uniformity bias is subsequently estimated
538 for individual masked brains. The preprocessing procedure outputs a skull-stripped bias-corrected image and a
539 companion binary brain mask for each subject.
540

541 **Figure 2. Preprocessing results.**

542 In this illustrative example, the original subject image (a) is bias corrected before (b) and after (e) skull stripping (d).
543 Note the improved bias field correction after skull stripping (f) with respect to the bias correction prior skull
544 stripping (c), especially in the ventral part of the brain and in the ventricles. Voxels intensity is represented in shades
545 of red to magnify image contrast.
546

547 **Figure 3. Automated anatomical labelling and cortical thickness estimation.**

548 Upper box: Anatomical labels of the MRI atlas are registered into each subject space via the study based template
549 through a combination of linear and diffeomorphic mapping, using *antsRegistration* and
550 *WarpImageMultiTransform*. A propagation of the labels from the MRI atlas to each subject space is then performed
551 via the study based template, followed by the estimation of the volume for each label. Lower box: Anatomical labels
552 of the cortical mantle in the subject space are merged together to build a unified cortical label. This cortical label and
553 subject brain mask of the subjects are used to create the inputs needed to estimate the cortical thickness using
554 *DiReCT*. The obtained cortical thickness maps are eventually warped again into the study based space and smoothed
555 for subsequent statistical comparison.
556

557 **Figure 4. VBM.**

558 Each preprocessed subject image is mapped on the study based template space through a combination of linear and
559 diffeomorphic mapping, using *antsRegistration* and *WarpImageMultiTransform*. Registered volumes are segmented
560 using the study based template priors. Grey matter probability maps for each subject are then modulated using
561 Jacobian maps obtained from the registration process and smoothed for subsequent statistical comparison.
562

563 **Figure 5. Study based template and tissue segmentation.**

564 Orthogonal slice view of a study based template of the B6 mice population obtained using the iterative
565 diffeomorphic registration process of the *buildtemplateparallel* script and its corresponding tissue segmentation (a).
566 The template is segmented using *Atropos* in 6 different tissue classes which are used as a-priori information for
567 individual estimation of gray matter in VBM. The different tissue classes of the template are combined to obtain
568 gray matter (b) and non gray matter components (c, white matter, plus ventricular regions and CSF).

Figure 6. Correlation plot between *DiReCT* outputs and manual measurements of cortical thickness.
Secondary motor (M2), secondary somatosensory (S2) and auditory cortex (Au) were chosen as representative cortical areas to validate our cortical thickness methodology. Representative measures from DiReCT and manual estimates are reported for selected cortical regions (middle panel). A correlation plot of manual and automatic measurements highlighted an excellent correspondence between the twee readouts in terms of Pearson's correlation ($r=0.99$; $p<0.001$).

Figure 7. Anatomical labelling.
The labels of the reference atlas employed are warped into subjects' space via the study based template using the combination of affine and diffeomorphic mapping obtained after the registration process. The registered labels permit to calculate volumes of brain areas of interest and perform t-tests between the mouse samples. (Cpu: caudoputamen; Th: thalamus; OB: olfactory bulbs; HP: hippocampus; Hyp: hypothalamus, CC: corpus callosum; OF: orbitofrontal cortex; RS: retrosplenial cortex; M1: primary motor cortex; V1: primary visual cortex; Rh: rhinal cortex). ** $p<.01$; *** $p<.001$.)

Figure 8. VBM.
Differences in local gray matter volumes are assessed combining gray matter probability maps and local Jacobian determinants. Statistical comparison ($p<.01$, threshold-free cluster enhancement followed by cluster-based thresholding) showed widespread and bilateral reductions in grey matter volumes across dorsofrontal, cingulate, retrosplenial, occipital and parietal cortex as well as in subcortical structures in BTBR compared to B6 controls. VBM highlighted also small bilateral foci of increased gray matter volume in the olfactory bulbs, in the medial pre-frontal and insular cortex, in the amygdala and in the dorsal hippocampus. (Cb: cerebellum; Cpu: caudoputamen; DHyp: dorsal hypothalamus; dPFC: dorsal prefrontal cortex; LTh: lateral thalamus; mPFC: medial prefrontal cortex; OB: olfactory bulbs; Rh: rhinal cortex; RS: retrosplenial cortex).

Figure 9. Cortical thickness estimation.
Three-dimensional rendering views of average cortical thickness in BTBR and B6 mice (a). Statistical comparison showed significant cortical thickness thinning ($p<0.01$, threshold-free cluster enhancement followed by cluster-based thresholding) in parietal, temporal and peri-hippocampal cortex of BTBR mice. Increased thickness was observed in medial prefrontal and anterior insular regions of this strain (b).

Figure S1. Segmentation of the study based template using six tissue classes provides accurate GM/WM separation.
A: Standard three-class segmentation of our ex vivo brains using Atropos did not produce an accurate GM/WM separation, with a great overestimation of white matter fraction. Anatomical template (left), plus the segmentation classes obtained with a three-cluster segmentation approach (WM, mixed WM/GM and GM matter maps, from left to right, respectively). B: The combined use of six independent segmentation classes leads to a more accurate

606 separation of GM and WM. The final GM map is the combined result of three GM classes (middle row). Additional
607 non-GM tissue can be obtained by merging the remaining three classes.
608
609 **Figure S2. Cortical thickness estimation.**
610 In lissencephalic brains, DiReCT measurement results in a string of voxels exhibiting constant thickness. This
611 appears in the form of parallel cortical "columns" in coronal brain slices clearly visible in the magnified view, where
612 colors represent the norm of the deformation field that is the estimated thickness.
613
614 **Figure S3. Optimization of registration parameters for anatomical labelling.**
615 Accuracy of registration (Dice coefficient) for varying registration parameters (window radius for cross correlation
616 and gradient steps). Top: as in Badea et al., (2012), we varied windows radius between 3 and 9 voxels. The chosen
617 value (5 voxels) produces a good performance in all the brain regions tested. Bottom: the gradient step parameter for
618 the symmetric normalization was varied between 0.10 and 2 voxels. The chosen parameter (0.5 voxels) produces a
619 good performance in all the tested regions.

620 **References**

621

622 Aggarwal M, Zhang J, Miller MI, Sidman RL, Mori S. Magnetic resonance imaging and micro-
623 computed tomography combined atlas of developing and adult mouse brains for stereotaxic
624 surgery. Neuroscience, 2009; 162: 1339-50.
625 Ashburner J, Friston KJ. Voxel-based morphometry--the methods. Neuroimage, 2000; 11: 805-
626 21.
627 Avants BB, Cook PA, Ungar L, Gee JC, Grossman M. Dementia induces correlated reductions
628 in white matter integrity and cortical thickness: a multivariate neuroimaging study with sparse
629 canonical correlation analysis. Neuroimage, 2010a; 50: 1004-16.
630 Avants BB, Epstein CL, Grossman M, Gee JC. Symmetric diffeomorphic image registration with
631 cross-correlation: Evaluating automated labeling of elderly and neurodegenerative brain.
632 Medical Image Analysis, 2008; 12: 26-41.
633 Avants BB, Tustison N, Song G. Advanced normalization tools (ANTS). Insight J, 2009.
634 Avants BB, Tustison NJ, Stauffer M, Song G, Wu B, Gee JC. The Insight ToolKit image
635 registration framework. Frontiers in neuroinformatics, 2014; 8.
636 Avants BB, Tustison NJ, Wu J, Cook PA, Gee JC. An open source multivariate framework for n-
637 tissue segmentation with evaluation on public data. Neuroinformatics, 2011; 9: 381-400.
638 Avants BB, Yushkevich P, Pluta J, Minkoff D, Korczykowski M, Detre J, Gee JC. The optimal
639 template effect in hippocampus studies of diseased populations. Neuroimage, 2010b; 49:
640 2457-66.
641 Badea A, Ali-Sharief AA, Johnson GA. Morphometric analysis of the C57BL/6J mouse brain.
642 Neuroimage, 2007; 37: 683-93.
643 Badea A, Gewalt S, Avants BB, Cook JJ, Johnson GA. Quantitative mouse brain phenotyping
644 based on single and multispectral MR protocols. Neuroimage, 2012; 63: 1633-45.
645 Borg J, Chereul E. Differential MRI patterns of brain atrophy in double or single transgenic mice
646 for APP and/or SOD. J Neurosci Res, 2008; 86: 3275-84.
647 Budin F, Hoogstoel M, Reynolds P, Grauer M, O'Leary-Moore SK, Oguz I. Fully automated
648 rodent brain MR image processing pipeline on a Midas server: from acquired images to
649 region-based statistics. Front Neuroinform, 2013; 7: 15.
650 Cahill LS, Laliberté CL, Ellegood J, Spring S, Gleave JA, van Eede MC, Lerch JP, Henkelman
651 RM. Preparation of fixed mouse brains for MRI. Neuroimage, 2012; 60: 933-9.
652 Chou C-H, Su M-C, Lai E. A new cluster validity measure and its application to image
653 compression. Pattern Analysis and Applications, 2004; 7: 205-20.
654 Cutuli D, Pagani M, Caporali P, Galbusera A, Laricchiuta D, Foti F, Neri C, Spalletta G,
655 Caltagirone C, Petrosini L. Effects of Omega-3 Fatty Acid Supplementation on Cognitive
656 Functions and Neural Substrates: A Voxel-Based Morphometry Study in Aged Mice. Frontiers
657 in aging neuroscience, 2016; 8.
658 Das SR, Avants BB, Grossman M, Gee JC. Registration based cortical thickness measurement.
659 Neuroimage, 2009; 45: 867-79.
660 Delatour B, Guegan M, Volk A, Dhenain M. In vivo MRI and histological evaluation of brain
661 atrophy in APP/PS1 transgenic mice. Neurobiol Aging, 2006; 27: 835-47.
662 Dice LR. Measures of the amount of ecologic association between species. Ecology, 1945; 26:
663 297-302.
664 Dodero L, Damiano M, Galbusera A, Bifone A, Tsaftsaris SA, Scattoni ML, Gozzi A.
665 Neuroimaging evidence of major morpho-anatomical and functional abnormalities in the
666 BTBR T+TF/J mouse model of autism. PLoS One, 2013; 8.
667 Dorr AE, Lerch JP, Spring S, Kabani N, Henkelman RM. High resolution three-dimensional brain
668 atlas using an average magnetic resonance image of 40 adult C57Bl/6J mice. Neuroimage,
669 2008; 42: 60-9.

670 Ellegood J, Babineau BA, Henkelman RM, Lerch JP, Crawley JN. Neuroanatomical analysis of
671 the BTBR mouse model of autism using magnetic resonance imaging and diffusion tensor
672 imaging. Neuroimage, 2013; 70: 288-300.
673 Friston KJ, Holmes AP, Worsley KJ, Poline JP, Frith CD, Frackowiak RS. Statistical parametric
674 maps in functional imaging: a general linear approach. Human brain mapping, 1994; 2: 189-
675 210.
676 Hutton C, De Vita E, Ashburner J, Deichmann R, Turner R. Voxel-based cortical thickness
677 measurements in MRI. Neuroimage, 2008; 40: 1701-10.
678 Jenkinson M, Beckmann CF, Behrens TE, Woolrich MW, Smith SM. Fsl. Neuroimage, 2012; 62:
679 782-90.
680 Jia H, Yap PT, Wu G, Wang Q, Shen D. Intermediate templates guided groupwise registration
681 of diffusion tensor images. Neuroimage, 2011; 54: 928-39.
682 Johnson GA, Ali-Sharief A, Badea A, Brandenburg J, Cofer G, Fubara B, Gewalt S, Hedlund
683 LW, Upchurch L. High-throughput morphologic phenotyping of the mouse brain with magnetic
684 resonance histology. Neuroimage, 2007; 37: 82-9.
685 Johnson GA, Badea A, Brandenburg J, Cofer G, Fubara B, Liu S, Nissanov J. Waxholm space:
686 an image-based reference for coordinating mouse brain research. Neuroimage, 2010; 53:
687 365-72.
688 Kim J, Avants B, Patel S, Whyte J, Coslett BH, Pluta J, Detre JA, Gee JC. Structural
689 consequences of diffuse traumatic brain injury: a large deformation tensor-based
690 morphometry study. Neuroimage, 2008; 39: 1014-26.
691 Klein A, Andersson J, Ardekani BA, Ashburner J, Avants B, Chiang M-C, Christensen GE,
692 Collins DL, Gee J, Hellier P. Evaluation of 14 nonlinear deformation algorithms applied to
693 human brain MRI registration. Neuroimage, 2009; 46: 786-802.
694 Klein A, Ghosh SS, Avants B, Yeo BT, Fischl B, Ardekani B, Gee JC, Mann JJ, Parsey RV.
695 Evaluation of volume-based and surface-based brain image registration methods.
696 Neuroimage, 2010; 51: 214-20.
697 Kovacevic N, Henderson JT, Chan E, Lifshitz N, Bishop J, Evans AC, Henkelman RM, Chen XJ.
698 A three-dimensional MRI atlas of the mouse brain with estimates of the average and
699 variability. Cereb Cortex, 2005; 15: 639-45.
700 Lassi G, Priano L, Maggi S, Garcia-Garcia C, Balzani E, El-Assawy N, Pagani M, Tinarelli F,
701 Giardino D, Mauro A. Deletion of the Snord116/SNORD116 Alters Sleep in Mice and Patients
702 with Prader-Willi Syndrome. Sleep, 2015.
703 Lee D, Ruffins S, Ng Q, Sane N, Anderson S, Toga A. MBAT: a scalable informatics system for
704 unifying digital atlasing workflows. BMC Bioinformatics, 2010; 11: 1471-2105.
705 Lee J, Ehlers C, Crews F, Niethammer M, Budin F, Paniagua B, Sulik K, Johns J, Styner M,
706 Oguz I. Automatic cortical thickness analysis on rodent brain. Proc Soc Photo Opt Instrum
707 Eng, 2011; 15: 7962481-79624811.
708 Lerch JP, Carroll JB, Dorr A, Spring S, Evans AC, Hayden MR, Sled JG, Henkelman RM.
709 Cortical thickness measured from MRI in the YAC128 mouse model of Huntington's disease.
710 Neuroimage, 2008; 41: 243-51.
711 Lerch JP, Gazdzinski L, Germann J, Sled JG, Henkelman RM, Nieman BJ. Wanted dead or
712 alive? The tradeoff between in-vivo versus ex-vivo MR brain imaging in the mouse. Front
713 Neuroinform, 2012; 6: 6.
714 Lerch JP, Sled JG, Henkelman RM. MRI phenotyping of genetically altered mice. Magnetic
715 Resonance Neuroimaging. Springer, 2011a: 349-61.
716 Lerch JP, Yiu AP, Martinez-Canabal A, Pekar T, Bohbot VD, Frankland PW, Henkelman RM,
717 Josselyn SA, Sled JG. Maze training in mice induces MRI-detectable brain shape changes
718 specific to the type of learning. Neuroimage, 2011b; 54: 2086-95.
719 Li Q, Cheung C, Wei R, Hui ES, Feldon J, Meyer U, Chung S, Chua SE, Sham PC, Wu EX.
720 Prenatal immune challenge is an environmental risk factor for brain and behavior change

721 relevant to schizophrenia: evidence from MRI in a mouse model. PLoS One, 2009; 4: e6354.
722 Ma Y, Smith D, Hof PR, Foerster B, Hamilton S, Blackband SJ, Yu M, Benveniste H. In Vivo 3D
723 Digital Atlas Database of the Adult C57BL/6J Mouse Brain by Magnetic Resonance
724 Microscopy. Front Neuroanat, 2008; 2.
725 Maheswaran S, Barjat H, Bate ST, Aljabar P, Hill DL, Tilling L, Upton N, James MF, Hajnal JV,
726 Rueckert D. Analysis of serial magnetic resonance images of mouse brains using image
727 registration. Neuroimage, 2009a; 44: 692-700.
728 Maheswaran S, Barjat H, Rueckert D, Bate ST, Howlett DR, Tilling L, Smart SC, Pohlmann A,
729 Richardson JC, Hartkens T, Hill DL, Upton N, Hajnal JV, James MF. Longitudinal regional
730 brain volume changes quantified in normal aging and Alzheimer's APP x PS1 mice using
731 MRI. Brain Res, 2009b; 13: 19-32.
732 Minervini M, Rusu C, Damiano M, Tucci V, Bifone A, Gozzi A, Tsaftaris SA. Large-scale
733 analysis of neuroimaging data on commercial clouds with content-aware resource allocation
734 strategies. International Journal of High Performance Computing Applications, 2014:
735 1094342013519483.
736 Mueller S, Keeser D, Reiser MF, Teipel S, Meindl T. Functional and structural MR imaging in
737 neuropsychiatric disorders, part 2: application in schizophrenia and autism. AJNR Am J
738 Neuroradiol, 2012; 33: 2033-7.
739 Nestler EJ, Hyman SE. Animal models of neuropsychiatric disorders. Nat Neurosci, 2010; 13:
740 1161-9.
741 Nieman BJ, Bock NA, Bishop J, Chen XJ, Sled JG, Rossant J, Henkelman RM. Magnetic
742 resonance imaging for detection and analysis of mouse phenotypes. NMR Biomed, 2005; 18:
743 447-68.
744 Oguz I, Sonka M. LOGISMOS-B: layered optimal graph image segmentation of multiple objects
745 and surfaces for the brain. IEEE Trans Med Imaging, 2014; 33: 1220-35.
746 Pagani M, Bifone A, Gozzi A. Structural covariance networks in the mouse brain. Neuroimage,
747 2016.
748 Sannino S, Gozzi A, Cerasa A, Piras F, Scheggia D, Manago F, Damiano M, Galbusera A,
749 Erickson LC, De Pietri Tonelli D, Bifone A, Tsaftaris SA, Caltagirone C, Weinberger DR,
750 Spalletta G, Papaleo F. COMT Genetic Reduction Produces Sexually Divergent Effects on
751 Cortical Anatomy and Working Memory in Mice and Humans. Cereb Cortex, 2014; 21: 21.
752 Sawiak S, Wood N, Williams G, Morton A, Carpenter T. SPMMouse: A new toolbox for SPM in
753 the animal brain. ISMRM 17th Scientific Meeting & Exhibition, April, 2009: 18-24.
754 Sawiak SJ, Wood NI, Williams GB, Morton AJ, Carpenter TA. Voxel-based morphometry with
755 templates and validation in a mouse model of Huntington's disease. Magnetic Resonance
756 Imaging, 2013; 31: 1522-31.
757 Sforazzini F, Bertero A, Dodero L, David G, Galbusera A, Scattoni ML, Pasqualetti M, Gozzi A.
758 Altered functional connectivity networks in acallosal and socially impaired BTBR mice. Brain
759 Structure and Function, 2014a: 1-14.
760 Sforazzini F, Schwarz AJ, Galbusera A, Bifone A, Gozzi A. Distributed BOLD and CBV-
761 weighted resting-state networks in the mouse brain. Neuroimage, 2014b; 87: 403-15.
762 Squillace M, Dodero L, Federici M, Migliarini S, Errico F, Napolitano F, Krashia P, Di Maio A,
763 Galbusera A, Bifone A, Scattoni ML, Pasqualetti M, Mercuri NB, Usiello A, Gozzi A.
764 Dysfunctional dopaminergic neurotransmission in asocial BTBR mice. Transl Psychiatry,
765 2014; 4: e427.
766 Tucci V, Kleefstra T, Hardy A, Heise I, Maggi S, Willemsen MH, Hilton H, Esapa C, Simon M,
767 Buenavista MT, McGuffin LJ, Vizor L, Dodero L, Tsaftaris S, Romero R, Nillesen WN, Vissers
768 LE, Kempers MJ, Vulto-van Silfhout AT, Iqbal Z, Orlando M, Maccione A, Lassi G, Farisello P,
769 Contestabile A, Tinarelli F, Nieus T, Raimondi A, Greco B, Cantatore D, Gasparini L,
770 Berdondini L, Bifone A, Gozzi A, Wells S, Nolan PM. Dominant beta-catenin mutations cause
771 intellectual disability with recognizable syndromic features. J Clin Invest, 2014; 124: 1468-82.

772 Ullmann JF, Watson C, Janke AL, Kurniawan ND, Reutens DC. A segmentation protocol and
773 MRI atlas of the C57BL/6J mouse neocortex. Neuroimage, 2013; 78: 196-203.
774 Worsley KJ, Evans AC, Marrett S, Neelin P. A three-dimensional statistical analysis for CBF
775 activation studies in human brain. Journal of Cerebral Blood Flow and Metabolism, 1992; 12:
776 900-.
777 Wu K-L, Yang M-S. A cluster validity index for fuzzy clustering. Pattern Recognition Letters,
778 2005; 26: 1275-91.
779 Xie Z, Yang D, Stephenson D, Morton D, Hicks C, Brown T, Bocan T. Characterizing the
780 regional structural difference of the brain between tau transgenic (rTg4510) and wild-type
781 mice using MRI. Med Image Comput Comput Assist Interv, 2010; 13: 308-15.
782 Yushkevich PA, Piven J, Hazlett HC, Smith RG, Ho S, Gee JC, Gerig G. User-guided 3D active
783 contour segmentation of anatomical structures: significantly improved efficiency and reliability.
784 Neuroimage, 2006; 31: 1116-28.
785 Zhang J, Peng Q, Li Q, Jahanshad N, Hou Z, Jiang M, Masuda N, Langbehn DR, Miller MI, Mori
786 S, Ross CA, Duan W. Longitudinal characterization of brain atrophy of a Huntington's disease
787 mouse model by automated morphological analyses of magnetic resonance images.
788 Neuroimage, 2010; 49: 2340-51.
789
790

Figure 1
Click here to download high resolution image

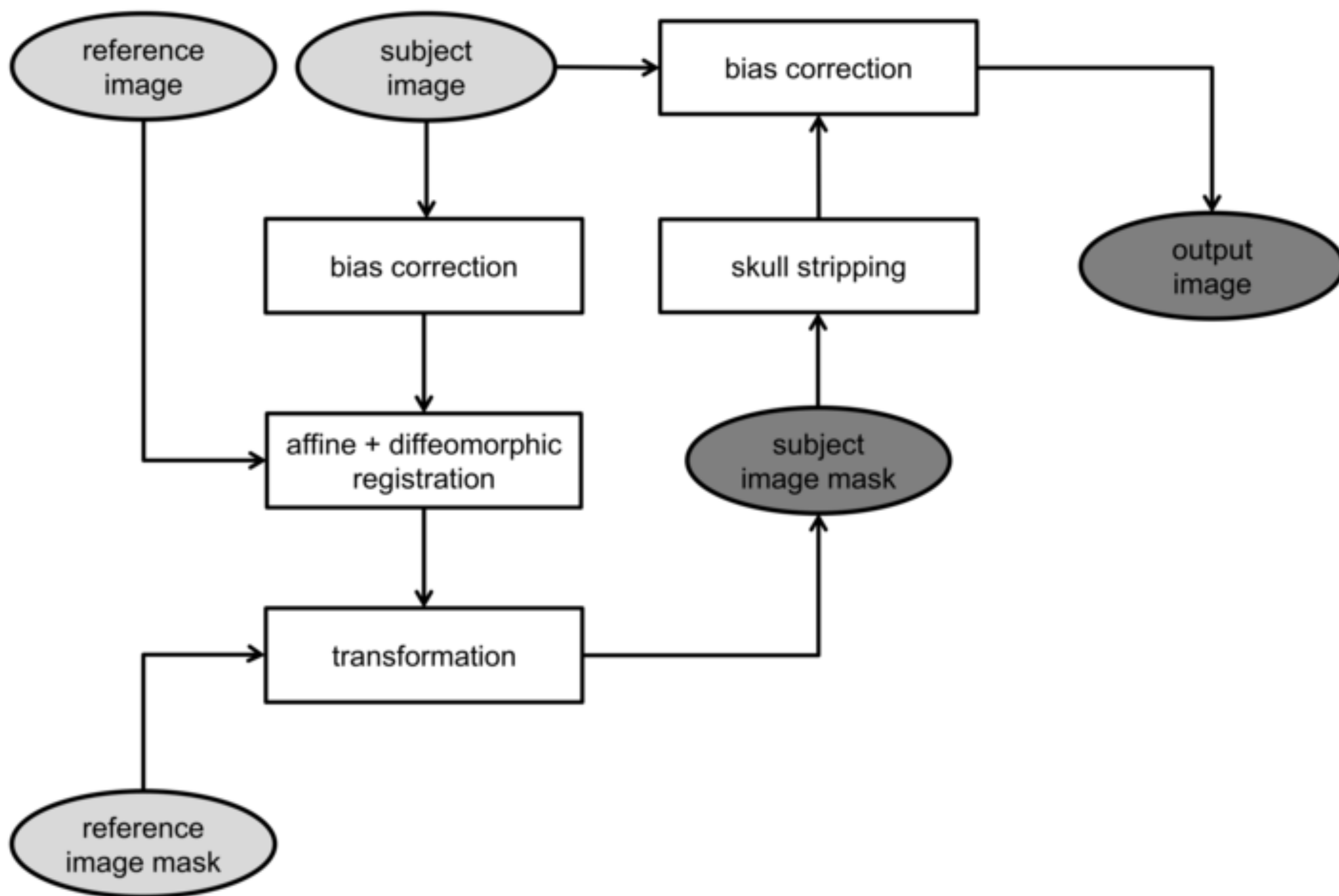

Figure 2
Click here to download high resolution image

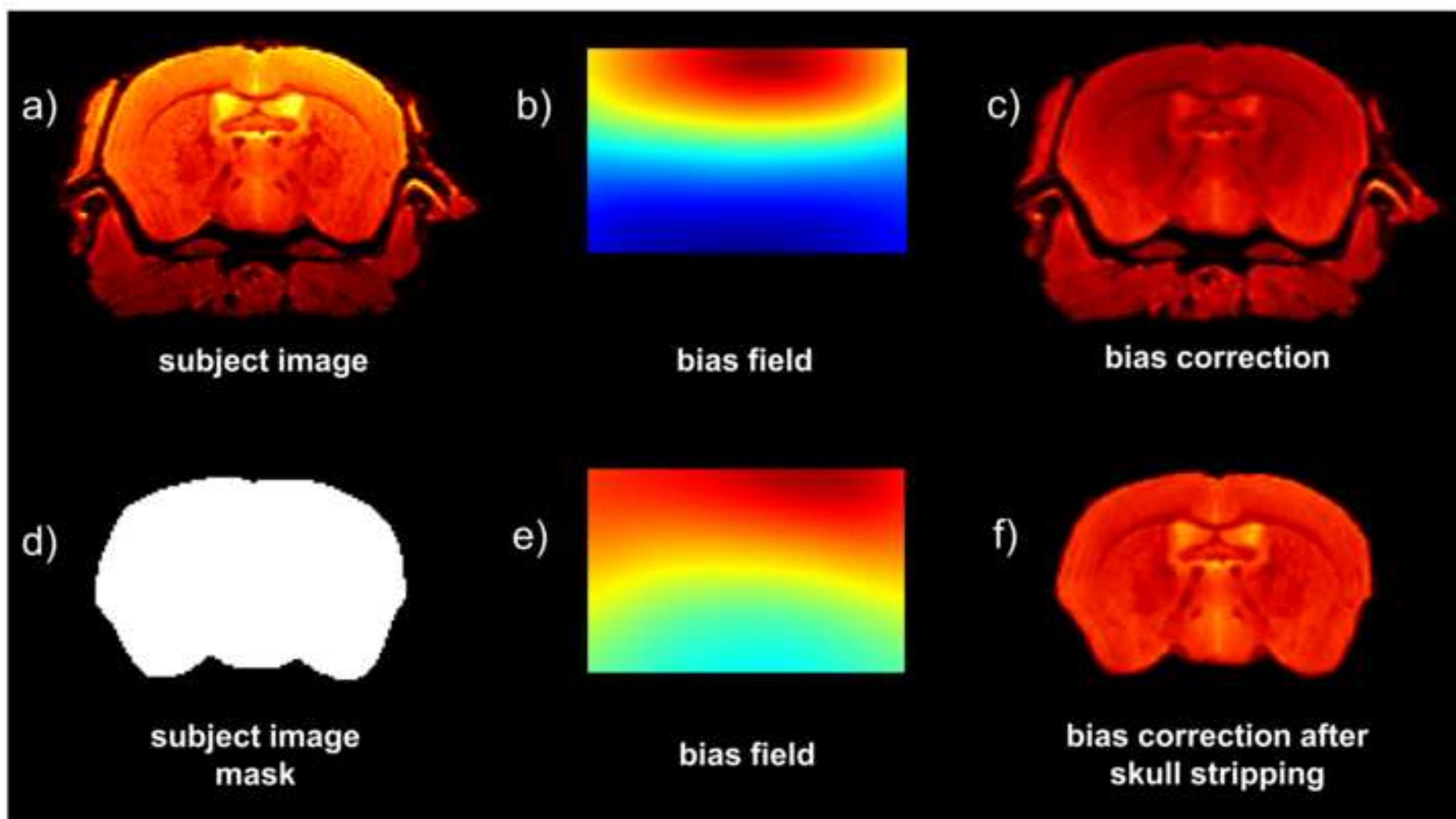

Figure 3
Click here to download high resolution image

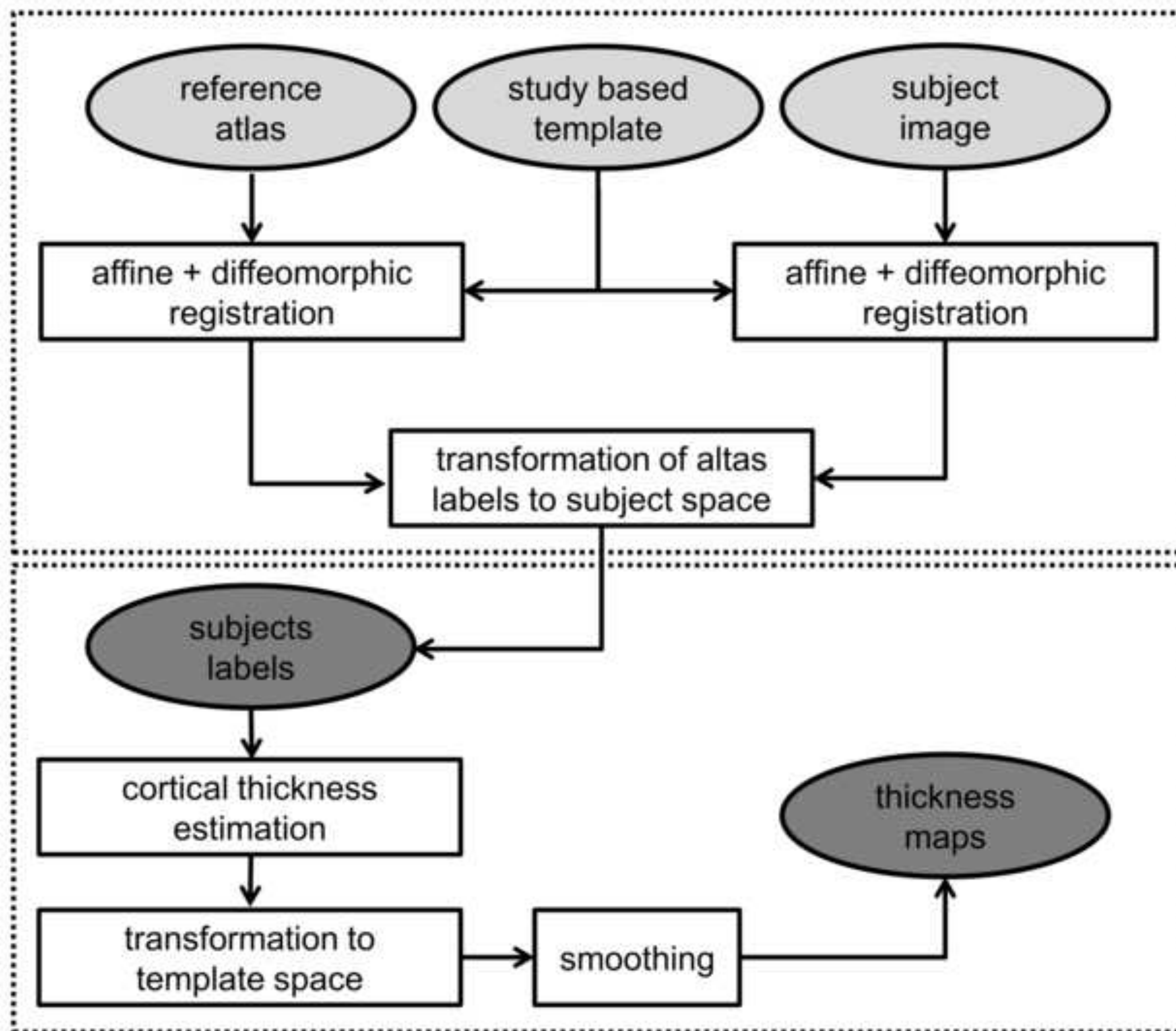

Figure 4
Click here to download high resolution image

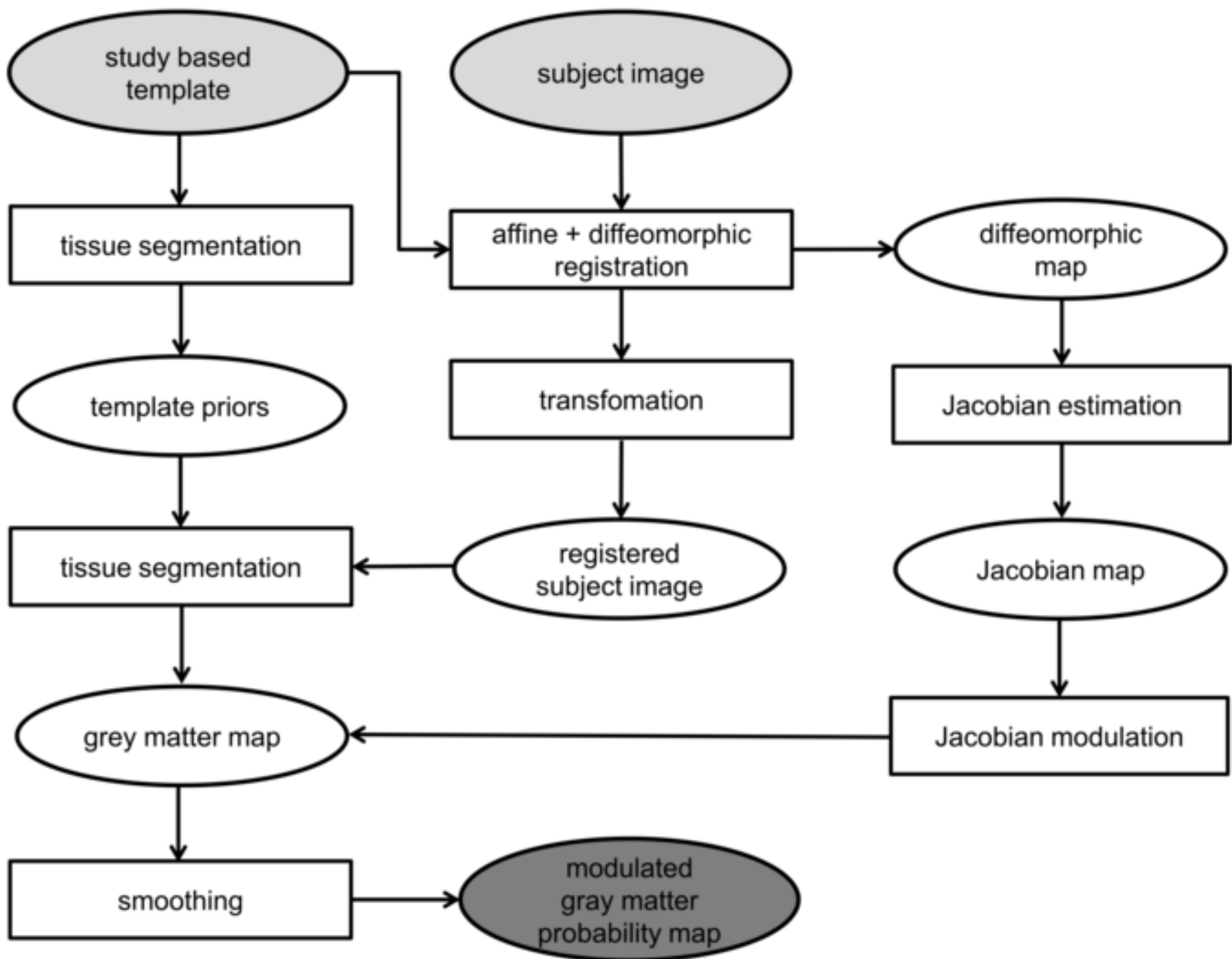

Figure 5

Click here to download high resolution image

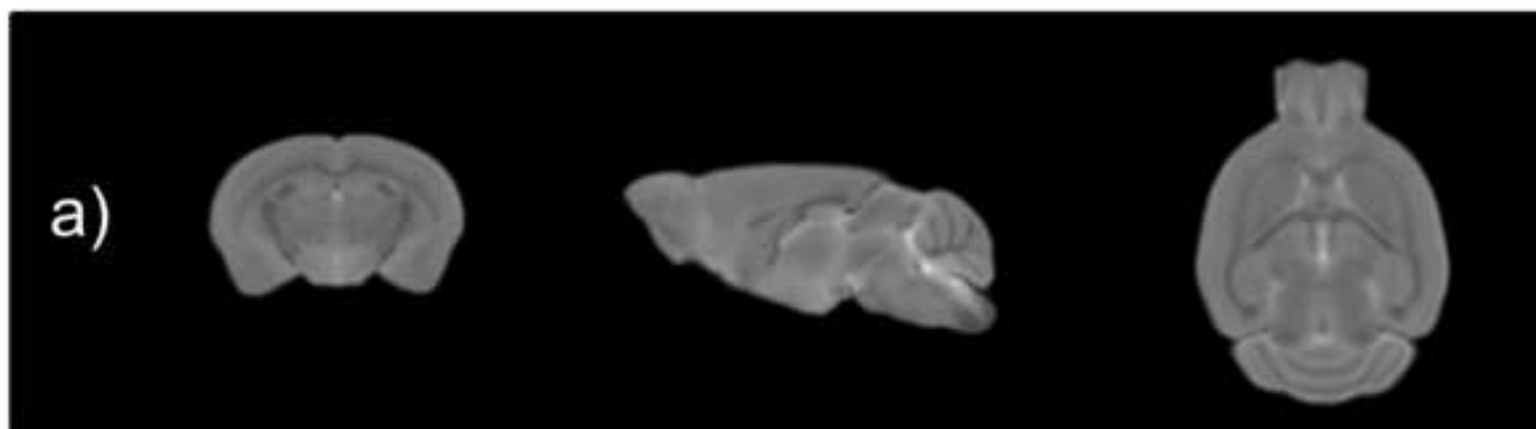

Figure 6

Click here to download high resolution image

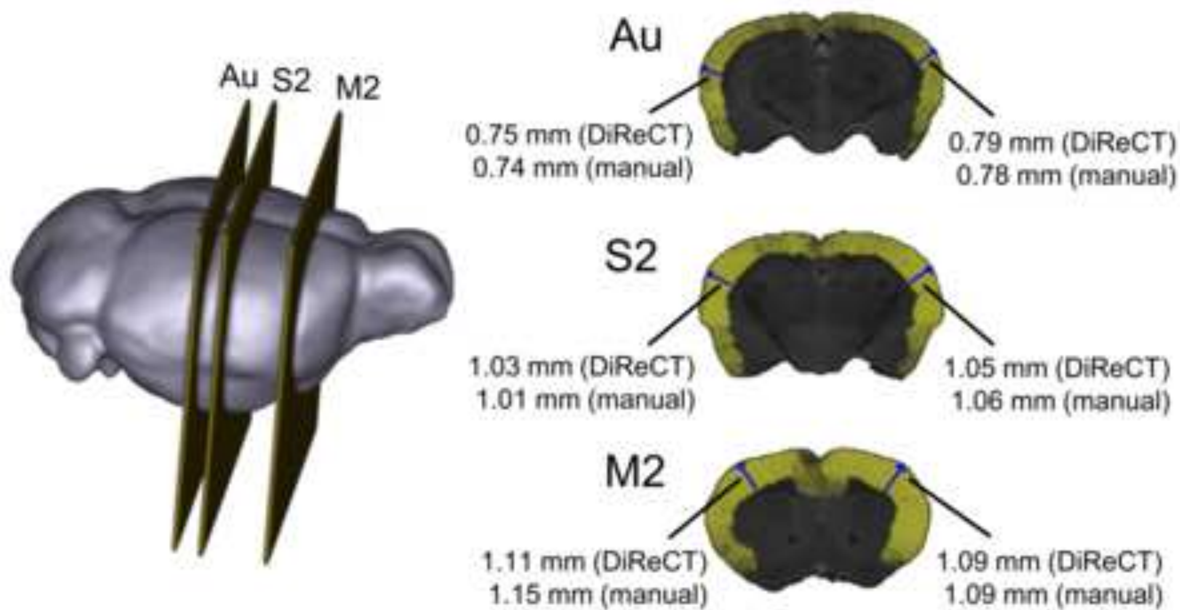

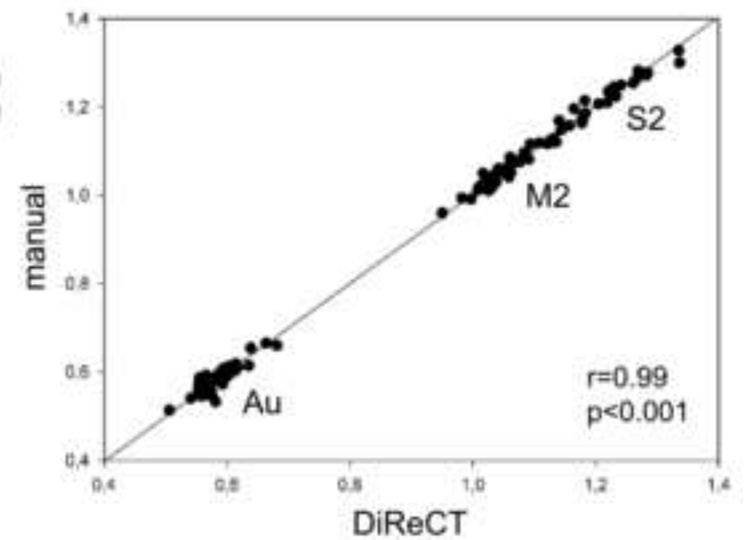

Figure 7

Click here to download high resolution image

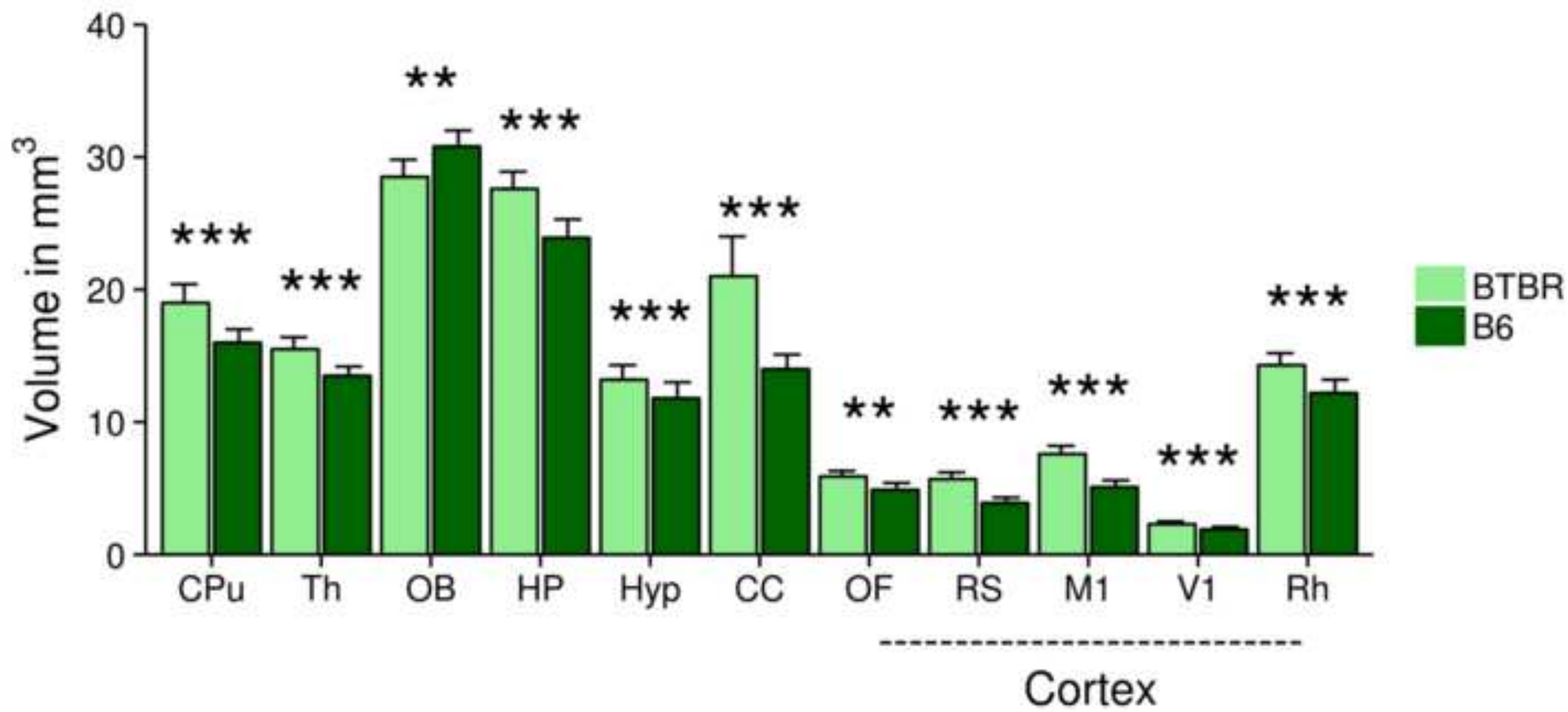

Figure 8

Click here to download high resolution image

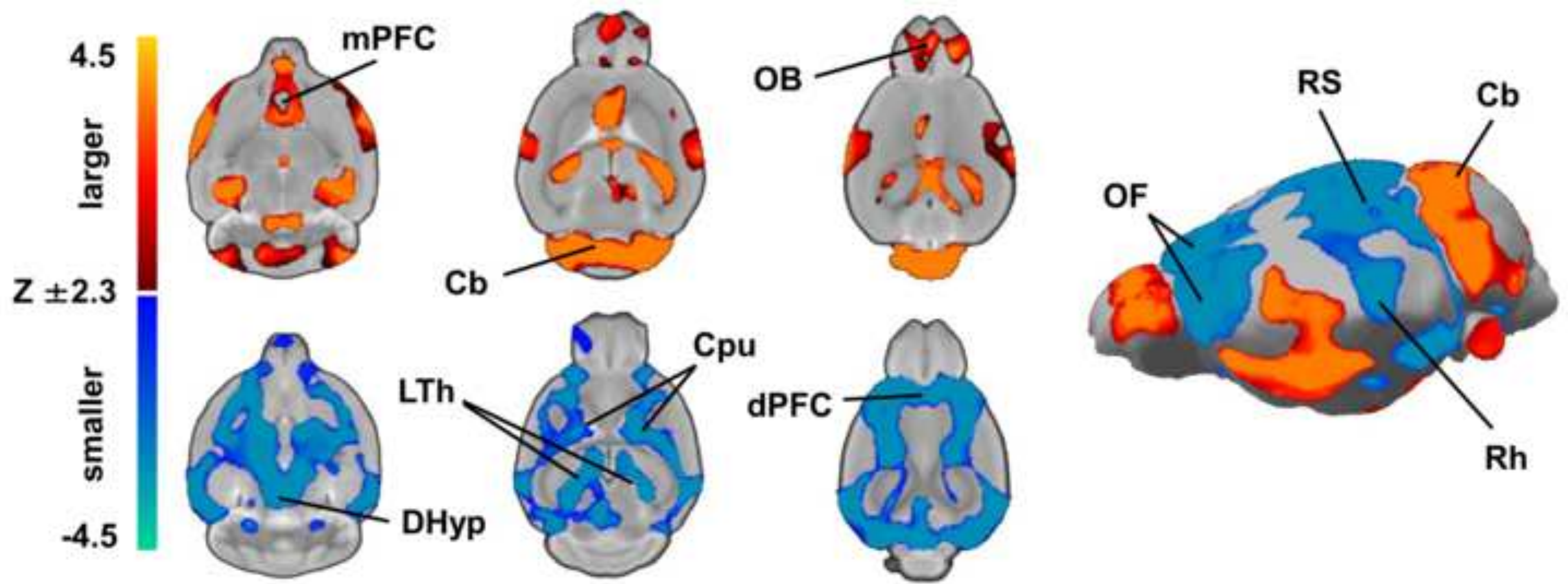

Figure 9
Click here to download high resolution image

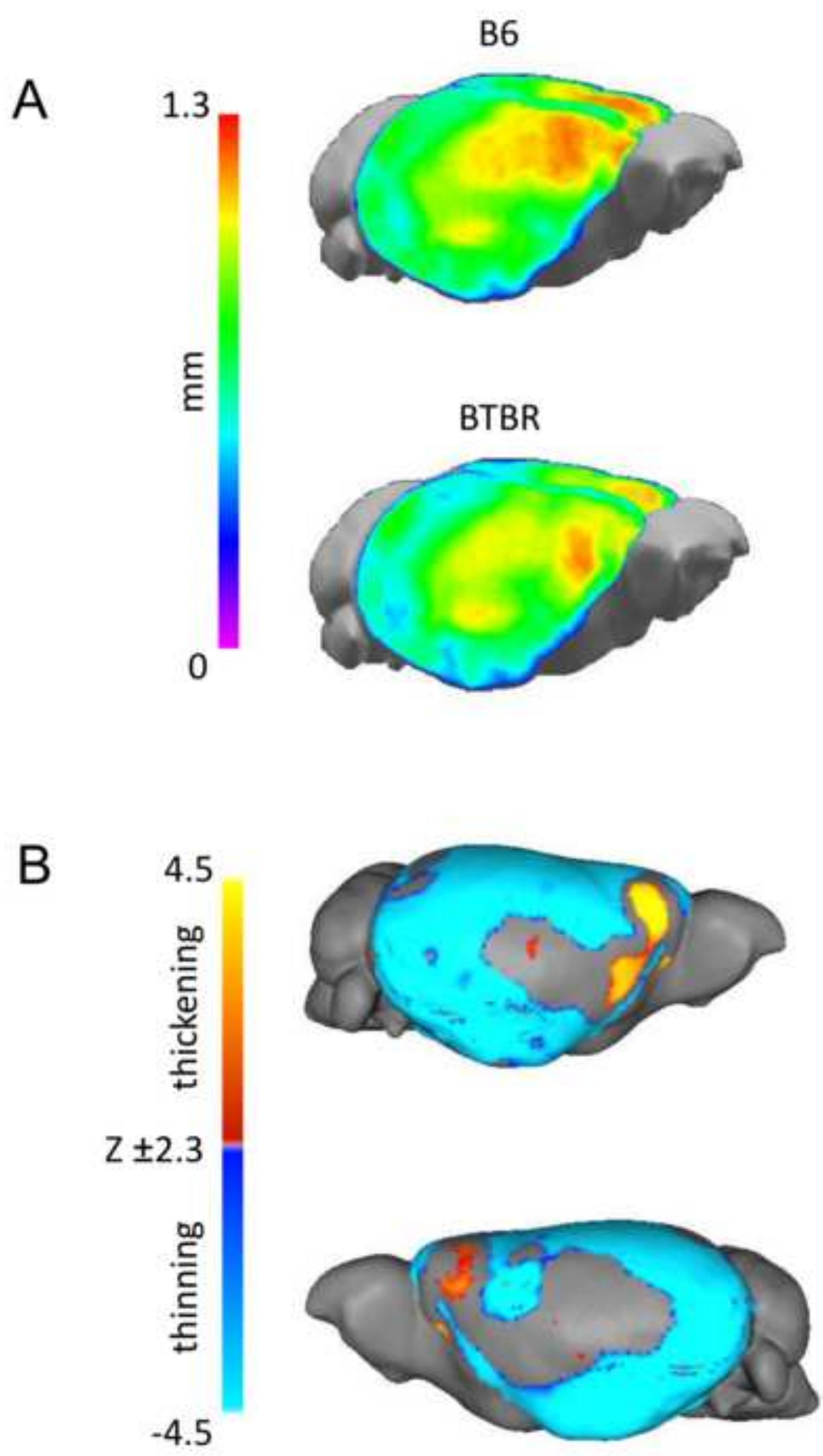

Figure S1

Click here to download high resolution image

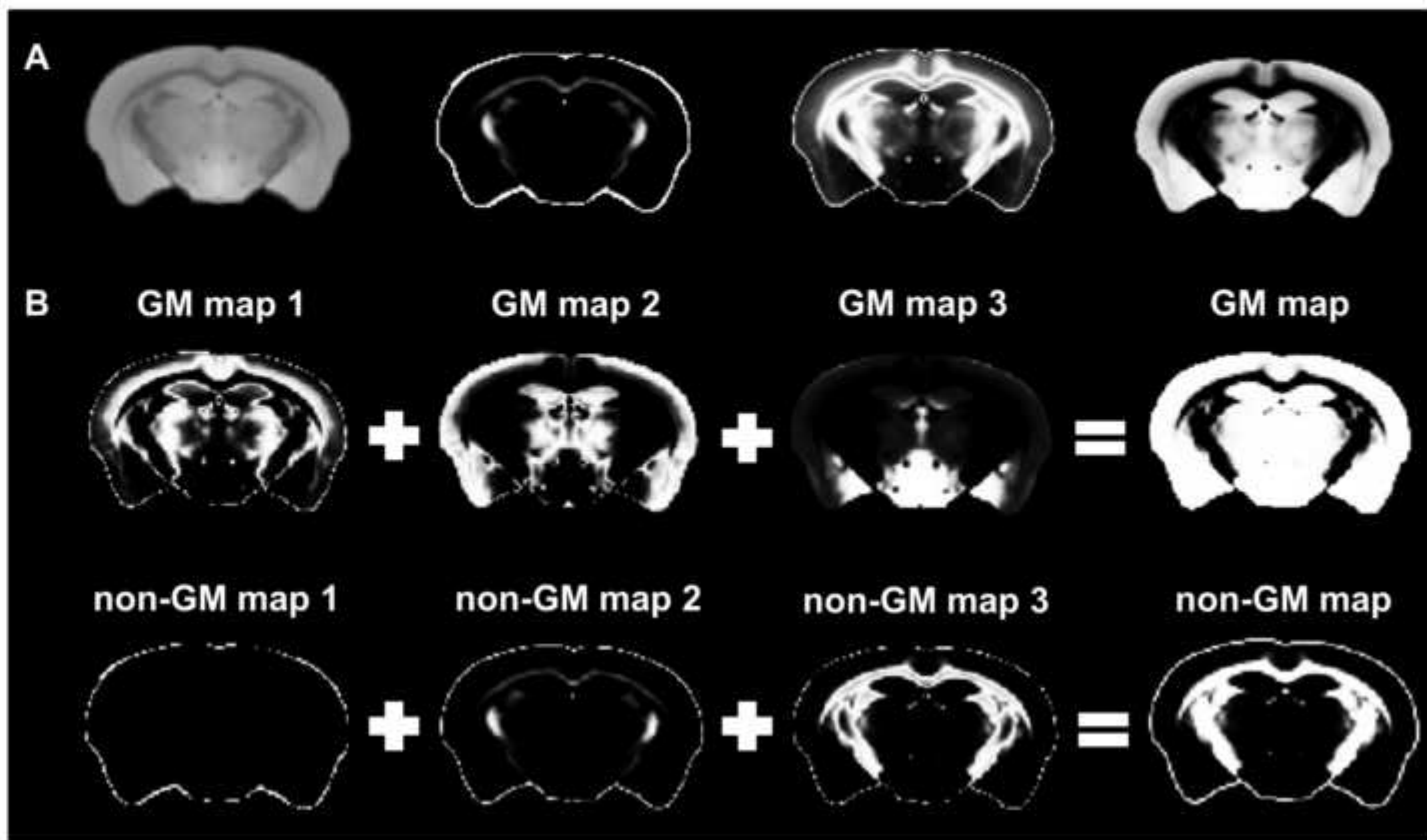

Figure S2

Click here to download high resolution image

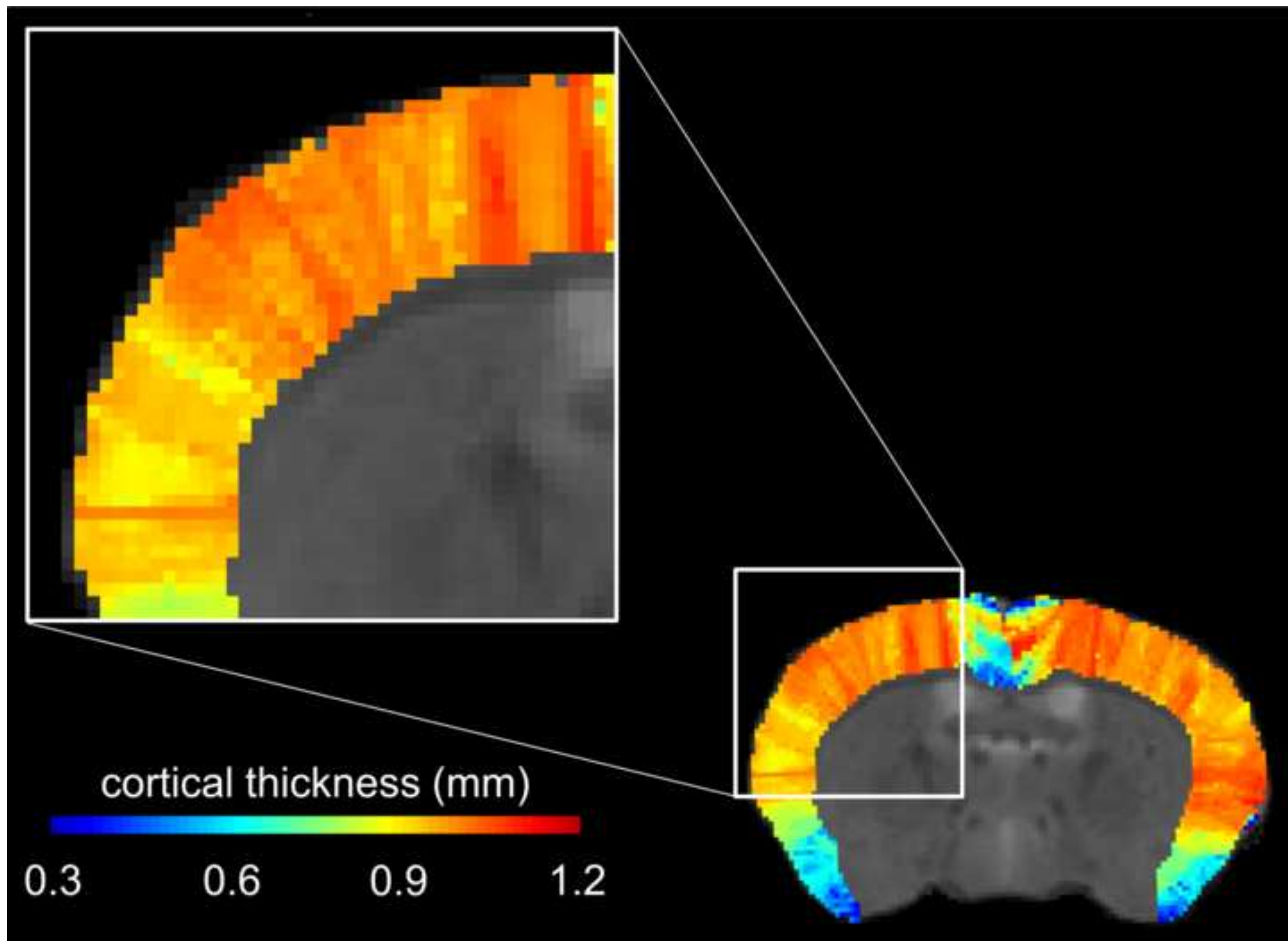

Figure S3

Click here to download high resolution image